

# In-flight aeroelastic measurement technique development

Alpheus W. Burner<sup>\*a</sup>, William A. Lokos<sup>b</sup>, Danny A. Barrows<sup>a</sup>

<sup>a</sup>NASA Langley Research Center, MS 236, Hampton, VA, USA 23681-2199;

<sup>b</sup>NASA Dryden Flight Research Center, MS 48202A, Edwards, CA, USA 93523-0273

## ABSTRACT

The initial concept and development of a low-cost, adaptable method for the measurement of static and dynamic aeroelastic deformation of aircraft during flight testing is presented. The method is adapted from a proven technique used in wind tunnel testing to measure model deformation, often referred to as the videogrammetric model deformation (or VMD) technique. The requirements for in-flight measurements are compared and contrasted with those for wind tunnel testing. The methodology for the proposed measurements and differences compared with that used for wind tunnel testing is given. Several error sources and their effects are identified. Measurement examples using the new technique, including change in wing twist and deflection as a function of time, from an F/A-18 research aircraft at NASA's Dryden Flight Research Center are presented.

**Keywords:** Aeroelasticity, deformation, photogrammetry, videogrammetry, AAW, Active Aeroelastic Wing, wing deflection

## 1. INTRODUCTION

Static and dynamic structural deformation are considered important aerospace vehicle characteristics necessary for accurate predictions; however, they are often not adequately known. Because current computational codes cannot sufficiently predict the full-scale aeroelastic performance of aircraft in flight, experimental aeroelastic measurements are needed. Currently, in-flight measurements of aeroelastic deformations are not routine, are costly, and require significant setup and aircraft adaptations. Special light emitting diodes (LEDs) are required that must be installed on the aerodynamic surfaces of interest for a limited amount of testing<sup>1-5</sup> with large, specialized, high-cost older measurement systems, such as the electro-optical Flight Deflection Measurement System (FDMS)<sup>1</sup> or the commercially available Optotrak® measurement system from Northern Digital Corporation.<sup>5</sup> Some aerodynamic surfaces, such as ailerons and leading edge slats, still are difficult to be measured with the older systems due to the requirement for LEDs, wiring, and special mounts that protrude above the aerodynamic surface.

Photogrammetry and image processing techniques have been used for the measurement of wind tunnel aeroelastic deformations at five major NASA ground-based facilities at Langley Research Center and Ames Research Center.<sup>6</sup> Wind tunnel applications from subsonic to supersonic include many types of models such as those used in the Advanced Subsonic Technology (AST) and High Speed Research (HSR) programs. The technique of choice developed to meet the needs of production wind tunnel testing with minimal impact to productivity is known as the videogrammetric model deformation (or VMD) technique. The technique uses *single-camera*, *single-view* photogrammetry coupled with image processing. The term "single-view" is used to distinguish between the single-camera, multiview technique, during which a single camera is moved about a static object to record multiple images that can then be used in a simultaneous solution to determine spatial coordinates. The single-camera, multiview technique is the technique of choice of the photogrammetric community.<sup>7</sup> The single-camera, single-view technique is not normally preferred for photogrammetric applications, but has several advantages for wind tunnel testing (and for flight testing). These advantages include: (1) only one camera is needed, reducing space and viewport requirements in the wind tunnel or on the aircraft; (2) the base separation of multiple cameras (with necessary suitable locations) is not a factor; and (3) the coordinate taken as known (to allow a single-camera solution) can usually be obtained with more accuracy pretest than is possible with multicamera photogrammetry during wind tunnel or in-flight data taking.

<sup>\*</sup>Alpheus.W.Burner@NASA.GOV; phone 757 864-4635; fax 757 864-4617

The use of trademarks or names of manufacturers in the report is for accurate reporting and does not constitute an official endorsement, either expressed or implied, of such products or manufacturers by the National Aeronautics and Space Administration.

Several initial examples of in-flight static aeroelastic measurements with the new technique are presented. Data were acquired from a flight-hardened video camera mounted on an F/A-18 research aircraft undergoing testing within NASA's Active Aeroelastic Wing (AAW) program<sup>8,9</sup> at Dryden Flight Research Center (DFRC). This F/A-18 aircraft is especially suited for this initial investigation because an equipment pod with available camera mounting space exists on the aircraft. In addition, the FDMS referred to earlier is available for comparison of deflection results. The AAW program is a joint program of the Air Force Research Laboratory (AFRL), DFRC, and The Boeing Company. The program started in August 1996 with a goal to develop flight-validated, active aeroelastic wing technology design guidance suitable for use on a future aircraft program. The program is the final step in a 20-year technology maturation process, which has its roots in the Active Flexible Wing program. The AAW F/A-18 project envisioned the application of in-flight structural deflection measurement from its earliest formation. Provisions were designed in the test aircraft to accommodate the Flight Deflection Measurement System (FDMS). This included a dorsally mounted receiver pod with window, 16 infrared LED targets on the upper left-hand wing surface with lead wires to a target driver box, a control unit box, power supplies, data telemetry interface circuit, and a cockpit-mounted on/off switch. As the FDMS installation was being designed, additional provisions were built in to support a developmental deflection measurement system. These provisions include additional space in the FDMS receiver pod and a longer window. Additionally, a pod heater was provided. These additional provisions make the AAW aircraft an ideal test-bed for the flight testing of new deflection measurement approaches.

The AAW F/A-18 research aircraft at DFRC is shown in figure 1. The camera pod housing the FDMS and video camera can be seen on the top of the fuselage overlooking the left wing. The camera pod as viewed from the right side of the aircraft is shown in figure 2, with a close-up of the camera pod highlighting the FDMS and video camera viewports depicted in figure 3. A planform of the aircraft showing the locations of the video camera, FDMS receivers, and FDMS targets (indicated with red circles) is shown in figure 4.

This paper describes initial efforts toward development of a new alternative low-cost method for aeroelastic deformation measurement that does not require LEDs and may eventually be more robust, accurate, and adaptable to measurement needs than current in-flight measurement systems.

## **2. DIFFERENCES BETWEEN WIND TUNNEL AND FLIGHT TESTING**

There are several notable differences between measuring wing deformation of a wind tunnel model compared with an aircraft in flight. For instance, the in-flight data camera would likely be mounted on the fuselage of the aircraft, thus the view presented to the data camera would be essentially the same throughout testing (except of course for any deformation or scale changes due to varying refractive index). For wind tunnel measurements the camera must typically be mounted on the test section wall. The pitch range of the model must be accommodated in the field-of-view so that the amount of the image plane occupied by the wing is necessarily reduced, which correspondingly reduces the accuracy of the measurements. For wind tunnel testing, a given target may move significantly on the image plane due to pitch-sweep testing, unlike the case for flight testing. In addition, the typical image plane motion during wind tunnel testing (due to the excursions in pitch during a run) makes it more critical to determine and properly account for optical lens distortion than for flight testing, where the motion on the image plane is confined to that produced by differential dynamics or the deformation itself. Unlike flight testing, wind tunnel testing requires the measurement of large angles because the local angles on the wing follow the model pitch angle relative to a fixed camera. Thus, it is common during wind tunnel testing to calibrate the optical measurement system in terms of angle with an onboard precision accelerometer at static test conditions. Such additional calibrations are probably not necessary for flight testing where the angular change is confined to a relatively small amount that is due to the aeroelastic deformation itself.

Wind tunnel measurements are further complicated by the need to accommodate and account for rigid body motion of the model due to sting bending induced by the overall aerodynamic loading on the model. Also for wind tunnel measurements, dynamics of the model can further exacerbate potential problems with the measurement. The measurement of wing deformation in flight is closer to a differential measurement, can make better use of the available image area, and is affected less by rigid body motion because the camera is on the body (fuselage). Dynamics may also be less of an issue for in-flight testing in one respect because the camera moves with the fuselage, thus any dynamics common to the fuselage and wing would tend to cancel.

Differences also occur with targeting. For most wind tunnel tests, retroreflective tape targets are used to provide very high-contrast targets to greatly increase the chances of successful automated image processing. (A notable exception to this is the National Transonic Facility at Langley Research Center, where a special polished paint technique has been developed to reduce the potentially harmful aerodynamic effect of the thicker and rougher surface-finish tape targets.) An example of a high-contrast image from a typical wind tunnel test is shown in figure 5. Another difference is that the wind tunnel model is typically viewed at an angle to the wing of about  $30^\circ$ , whereas for aircraft in flight, the data camera located on the fuselage would likely have an angle-of-view to the wing closer to  $10^\circ$  or less. Because the light return from retroreflective material drops significantly as the angle of incidence moves away from normal, the retroeffect for aircraft with a shallow angle of incidence would be reduced. One way around this would be to place the targets on raised tabs to orient the tape targets toward the camera; however, the potential aerodynamic disturbance would then be a consideration equivalent to that now encountered with the FDMS targets. Another aspect of retroreflective material that complicates their use for deformation measurements on aircraft in flight is the requirement for a light source near the camera. The space required for such a light source, along with its additional wiring, mounting, and operational concerns, limits the desirability of an additional light source for in-flight testing. The use of natural features or passive targets that do not require additional wiring or special mounting is very desirable for in-flight testing.

Another difference between wind tunnel and flight testing is the very nature of the tests themselves. It is common in wind tunnel testing to require that data be available at least within a few minutes after the completion of a run series. Thus, near real-time data processing and rapid final reduction are necessary for an effective and useful model deformation measurement system for a production wind tunnel. Flight testing, on the other hand, normally consists of an hour or so flight where, during the flight, there is usually no pressing need for near real-time deformation data. The desirable requirements for data processing and final reduction for in-flight measurements of wing deformation might be better expressed as “rapid, next-day delivery of reduced data.” Also, the very nature of the unknowns in flight testing make it desirable to record images for post-flight analyses rather than the procedure of capturing images, performing image processing, recording the results of image processing, and overwriting the images, as is commonly done during more well-defined wind tunnel testing. The recording of images for posttest processing is especially important during early phases of technique development. In fact, during the early stages of development of a wind tunnel model deformation measurement system, images were likewise recorded for postrun or posttest analyses in order to develop a databank of troublesome images for technique development and enhancement.

Finally, flight-hardened hardware is a major concern for any in-flight test technique. Flight hardware must be able to endure a variable and hostile environment and still continue to function. Ambient temperature can vary over a range of up to  $270^\circ\text{F}$  or more. Air pressure can go so low as to allow electrical circuits to arc. Structural vibrations can sometimes shake electrical or mechanical components to pieces. Moisture can be present as well as jet fuel. Further, flight systems must be able to run unattended.

### **3. DATA REDUCTION PROCEDURES FOR IN-FLIGHT MEASUREMENTS**

#### **3.1 Overall concept**

One of the long-term goals of this effort is to develop a test technique able to provide next-day, continuous, time-resolved aeroelastic results from takeoff to landing. It is envisioned that an image sequence of the entire flight will provide the raw data from which time-resolved deflection can be extracted. As mentioned earlier, a variation of the videogrammetric model deformation measurement technique used in wind tunnel testing offers promise for such in-flight measurements. Central to the extraction of meaningful image data that can be transformed to deflection is the applicability of automated image processing that is robust and requires little user intervention. In order to apply single-camera, single-view photogrammetry, which is the basis of the measurement, the pointing angles and location of the data camera must be determined in the aircraft coordinate system. This is accomplished with a well-known photogrammetric procedure known as space resection with assumed or known values of several camera parameters. Once all camera parameters and the pointing angles and location are known, two of three coordinates (with the third coordinate known) can then be computed from a single-camera view. To determine deflection, the vertical coordinates at a reference condition are subtracted from the vertical coordinates at the condition of interest. Angles are determined from the slope of computed coordinates in chordwise planes at the various spanwise locations where targets or suitable image patches exist. Local angles at various span stations at the reference condition are subtracted from the condition of interest to

yield the change in angle (induced twist) due to aeroelastic loading. An alternative approach to single-camera, single-view photogrammetry requiring resection is the determination of scale factors at each target (or image patch) location. This is essentially the approach used for the FDMS and, depending on the availability of targets with known 3D coordinates, may be desirable for some situations.

Two recording approaches are being investigated. The first approach uses a high-resolution (3 Megapixel) digital still camera for selected data samples. Mounting and other installation details are still underway for this camera. The second approach uses a standard resolution flight-hardened video camera for recording. This camera, normally used for surveillance of the left wing, provided the image sequences for the initial results reported here. These video data sets expedite test technique development with real-world flight-test data for evaluation.

### 3.2 Determining pointing angles and location of data camera

The first task in the data reduction procedure is to determine the location and pointing angles of the data camera in the aircraft coordinate system. This can be accomplished photogrammetrically with a process known as space resection, or simply resection. In resection, 2D image plane coordinates are mathematically compared with their known 3D object space coordinates (which defines the coordinate system). Nonlinear least squares is used to extract estimates of the Euler angles  $\omega$ ,  $\phi$ ,  $\kappa$  (defining the pointing angles of the data camera) and the location of the effective perspective center of the camera  $X_c$ ,  $Y_c$ ,  $Z_c$  as well as precision estimates of these computed quantities. The basic equations used for this computation are referred to as the collinearity equations.<sup>6</sup> The collinearity equations (1) are the most fundamental and important data reduction equations in photogrammetry. They express the ideal imaging relationship that the object point, perspective center, and image point should be on a straight line. In equations (1) below, the image coordinates  $x$ ,  $y$  have been corrected for optical lens distortion<sup>10</sup> or the distortion is negligible. Unlike wind tunnel testing, the image motion of targets (or a given image patch) is small compared with wind tunnel testing; therefore, lens distortion has much less effect on the results and is ignored for these initial efforts. The photogrammetric principal point, which can be thought of as the point of symmetry for imaging, is represented by  $x_p$ ,  $y_p$ , the principal distance is represented by  $c$ , and the object space location of each target is represented by  $X$ ,  $Y$ ,  $Z$ . The principal distance is the perpendicular image distance from the rear perspective center to the image plane and would ideally be equal to the effective focal length if the lens were focused on infinity. If the lens is focused on a near object (as for the examples presented here) the principal distance will be a little longer than the effective focal length and can be estimated from the well-known Gaussian object-image relationship among object distance, image distance, and effective focal length. The location of the perspective center is represented by  $X_c$ ,  $Y_c$ ,  $Z_c$ .

$$\begin{aligned} x &= x_p - c \left[ \frac{m_{11}(X - X_c) + m_{12}(Y - Y_c) + m_{13}(Z - Z_c)}{m_{31}(X - X_c) + m_{32}(Y - Y_c) + m_{33}(Z - Z_c)} \right] \\ y &= y_p - c \left[ \frac{m_{21}(X - X_c) + m_{22}(Y - Y_c) + m_{23}(Z - Z_c)}{m_{31}(X - X_c) + m_{32}(Y - Y_c) + m_{33}(Z - Z_c)} \right] \end{aligned} \quad (1)$$

The Euler angles  $\omega$ ,  $\phi$ ,  $\kappa$ , which orient the image plane to the coordinate system of interest about the  $X$ ,  $Y$ ,  $Z$  axes, respectively, are used to compute the nine elements of the rotation matrix given by equation (2).

For the initial efforts presented here, the following assumptions were made. The principal point,  $x_p$ ,  $y_p$ , was approximated as a fixed location near the center of the digital image extracted from the DVD recordings at a resolution of 704 horizontal pixels by 480 vertical pixels. In pixel space, the coordinates for  $x_p$ ,  $y_p$  were taken to be 352, 240, which during the conversion from pixel space to millimeters on the image plane corresponded to a value of  $x_p$ ,  $y_p$  = (0, 0). The principal distance was estimated to be 16.08 mm based on an assumed focus toward the outboard portion of the wing and an effective focal length of 16 mm. The results are only weakly dependent on the actual value of the principal distance used due to the differential nature of the computations to establish the difference in  $Z$  (or in angle) from a given measurement condition to another. It is common for wind tunnel testing to perform a lens calibration to determine principal distance, principal point, and lens distortion (both radial and asymmetric).<sup>10</sup> However, for flight testing, motion of targets on the image plane is confined to localized regions (in fact, inboard image areas are effectively stationary), and additional lens calibration is probably not necessary. A sensitivity analysis is suggested to determine the

effects of the various lens calibration coefficients on the results in order to ascertain the value of additional lens calibration for a particular project.

$$\begin{aligned}
m_{11} &= \cos \phi \cos \kappa \\
m_{12} &= \sin \omega \sin \phi \cos \kappa + \cos \omega \sin \kappa \\
m_{13} &= -\cos \omega \sin \phi \cos \kappa + \sin \omega \sin \kappa \\
m_{21} &= -\cos \phi \sin \kappa \\
m_{22} &= -\sin \omega \sin \phi \sin \kappa + \cos \omega \cos \kappa \\
m_{23} &= \cos \omega \sin \phi \sin \kappa + \sin \omega \cos \kappa \\
m_{31} &= \sin \phi \\
m_{32} &= -\sin \omega \cos \phi \\
m_{33} &= \cos \omega \cos \phi
\end{aligned} \tag{2}$$

With the principal distance and principal point assumed, and known  $X, Y, Z$  associated with each target or image patch location, the remaining unknowns in equations (1), namely  $\omega, \phi, \kappa$  and  $X_c, Y_c, Z_c$ , are then solved for with an iterative nonlinear least-squares solution, which requires initial start values. For the examples presented below, the FDMS targets were used as reference because their locations had been measured with a precision theodolite before flight testing began. An image from level flight was used to establish the approximate pointing angles and location of the video camera. The image locations were determined manually in MATLAB® by setting a cursor at each target location on the digital image of interest. (Note that one minor difference in MATLAB® compared with the more usual convention is that the upper left pixel has a value of 1,1 instead of 0,0.) The pixel coordinates (with the origin to the upper left of the image),  $x_{pix}, y_{pix}$ , were converted to units of millimeters,  $x_{mm}, y_{mm}$ , with the following equations:

$$\begin{aligned}
x_{mm} &= (x_{pix} - x_o) S_h \\
y_{mm} &= -(y_{pix} - y_o) S_v
\end{aligned} \tag{3}$$

where  $x_o, y_o$  locate the principal point in pixel space (352, 240) and  $S_h$  and  $S_v$  are the effective horizontal and vertical pixel spacings of the digital imagery. The effective pixel spacings  $S_h$  and  $S_v$  were adjusted from repeated photogrammetric resections until the computed location of the video camera from resection was in reasonable agreement with its assumed location (to within a tolerance of several centimeters). An additional constraint that  $S_h = (639/703) S_v$  was initially applied to account for the digital conversion at  $704 \times 480$  instead of the more common square pixel format of  $640 \times 480$ . The horizontal pixel spacing was further adjusted to minimize image plane resection residuals to yield a final estimate for  $S_h, S_v$  of 0.02484, 0.028 mm. Because differential measurements are being made from image coordinates that differ little from condition to condition, the exact value of the horizontal and vertical pixel spacings is not as critical as for multicamera photogrammetric solutions or single-camera, single-view solutions where there is relatively large motion on the image plane (such as that which occurs during wind tunnel testing).

During initial attempts at resection on the wing during level flight, an incorrect local minimum solution was found rather than the global minimum that corresponds to the desired solution. (In nonlinear least squares an incorrect local minimum solution, instead of the correct global minimum solution, can be found if the start values for the iterative process are not sufficiently close to the final correct values.) This is illustrated in figure 6 where the manually determined image coordinates of the FDMS targets are indicated with  $\circ$ 's and the computed image plane coordinates (transformed to pixels) from the incorrect local minimum solution are indicated with  $+$ 's. The computed coordinates were found by applying the collinearity equations (1), with the pointing angles and camera position found from resection, to the 3D spatial coordinates of the FDMS target housings and then converting the image coordinates from millimeters to pixels for final plotting. Once the start values for the resection were tweaked to closer to the correct values, the correct global minimum was found, as indicated by the near overlap of the  $\circ$ 's and  $+$ 's in figure 7. The image plane residuals corresponding to figure 7 are depicted in figure 8 as vectors. Such plots as figures 6 and 7 were found to be very useful during initial resection efforts.

### 3.3 Single-camera, single-view photogrammetric solution

The collinearity equations can be recast in linear form as:

$$\begin{aligned} a_1X + a_2Y + a_3Z &= a_1X_c + a_2Y_c + a_3Z_c \\ a_4X + a_5Y + a_6Z &= a_4X_c + a_5Y_c + a_6Z_c \end{aligned} \quad (4)$$

where

$$\begin{aligned} a_1 &= (x - x_p) m_{32} + c m_{12} \\ a_2 &= (x - x_p) m_{31} + c m_{11} \\ a_3 &= (x - x_p) m_{33} + c m_{13} \\ a_4 &= (y - y_p) m_{32} + c m_{22} \\ a_5 &= (y - y_p) m_{31} + c m_{21} \\ a_6 &= (y - y_p) m_{33} + c m_{23} \end{aligned} \quad (5)$$

If two or more cameras image a single point and  $a_1$  through  $a_6$  (containing coefficients  $x_p, y_p, c, \omega, \phi, \kappa$ ) and  $X_c, Y_c, Z_c$  are known, then the spatial coordinates  $X, Y, Z$  can be determined with linear least squares. This is the basis of photogrammetric intersection, or triangulation. If one of the spatial coordinates is known, such as the semispan location of image points ( $X$ ), then a single-camera image of a point results in two equations in two unknowns. With  $X$  known,  $Y$  (fuselage station) and  $Z$  (vertical) can be found with the following algebraic solution:

$$\begin{aligned} Y &= Y_c + \frac{(X - X_c)(a_2a_6 - a_5a_3)}{(a_4a_3 - a_1a_6)} \\ Z &= Z_c - \frac{(Y - Y_c)a_1 + (X - X_c)a_2}{a_3} \end{aligned} \quad (6)$$

The primary advantages of this single-camera, single-view technique are: (1) only one camera is needed, reducing space and viewport requirements on the aircraft; (2) the base separation of multiple cameras (with necessary suitable locations) is not a factor; and (3) the coordinate taken as known (to allow a single-camera solution) can usually be obtained with more accuracy pretest than is possible with multiview photogrammetry during in-flight data taking. When comparing multicamera with single-camera techniques, it should be noted that variance in the photogrammetrically computed  $X$ -coordinate of a multicamera measurement will lead to variance in the more critical  $Z$ -values. This is not an issue with the single-camera, single-view technique because the  $X$ -values are determined to greater precision with theodolites prior to testing. The bias errors in  $Y$  and  $Z$  due to error in  $X$  tend to cancel upon the subtraction that is inherent in differential measurements (runway-to-flight, level-flight-to-maneuver, etc.). Additional uncertainty considerations for the technique when used for wind tunnel testing, including the effect of changes in the known coordinate  $X$  due to bending, are addressed in reference 10 (where the known semispan coordinate is represented as  $Y$  instead of  $X$ , and  $X$  and  $Z$  are solved for instead of  $Y$  and  $Z$  as shown here).

Once the  $Y$  and  $Z$  coordinates are computed for a given semispan location  $X$ , a slope angle can be computed in the  $YZ$  plane by either least squares for multiple image coordinates or directly when there are only two targets per semispan. This angle, designated as the videogrammetric angle  $\theta_\eta$ , is given at each normalized semispan location  $\eta$  by:

$$\theta_\eta = \tan^{-1} \frac{\Delta Z_\eta}{\Delta Y_\eta} \quad (7)$$

Thus, the data extracted from the flight images would consist of angles at each semispan station (if more than one target per semispan) and  $Z$ -deflection values for each target or image patch. The reference condition (e.g., runway or level

flight)  $Z$ -values or angles are then subtracted from the condition of interest to determine the change in deflection or angle (induced twist) from the reference to that condition.

Figure 9 shows the error in  $Z$  using the single-camera, single-view computation (equations (5) and (6)) where the image plane coordinates used for the resection are used as input along with the known  $X$ -values of the FDMS target housings to compute  $Y$  and  $Z$ . The known  $Z$ -values of the FDMS targets from the theodolite measurements are then subtracted from the computed  $Z$ -values to yield the errors, which are plotted as vectors. To further assess the potential error, the effects on the  $Z$ -computation of a 1-pixel error in both vertical and horizontal image coordinates are depicted in figures 10 and 11, respectively. Note that, as expected, the error grows toward the wing tip because the scale decreases toward the tip. Also note that the method is about 10 times less sensitive to errors in horizontal image coordinates than for vertical image plane coordinates because the vertical image coordinate is nearly parallel to the  $Z$ -spatial coordinate in the object field.

### 3.4 Image processing and targeting considerations

In order to extract useful spatial information from a digital image in a timely manner, some variation of image processing is needed. The basic methods under consideration for this developmental effort are centroiding of discrete targets or targetlike features, edge detection, and image correlation of natural features. Reported here are the initial attempts at the first two of these. Subpixel image correlation, although not presented here, offers perhaps the best potential for future efforts because the use of correlation of natural features may obviate the need for any targets to be applied to the wing. In addition, nearly global coverage of the wing may be possible using natural features. It is expected that for regions of the wing where natural features are nondescript, tape targets may be necessary to obtain data in those regions, even when using image correlation.

For the initial efforts for resection outlined above, and for the examples of FDMS target deflection, it was simplest and most straightforward to manually select the image coordinates that correspond to the FDMS target housing locations. Efforts to extract the image coordinates with binarization, segmentation, and centroiding were only partially successful due to the very low contrast and low resolution of the video images. In addition, the images have enough background clutter surrounding a given target location to make the application of automated image processing difficult. The contrast of the target housings also varies drastically with time, sometimes actually switching sign, depending on the location of the Sun with respect to the wing. Given the mostly white nature of the wing, it is expected that the best chance of success with automated image processing would occur with flat-black targets of sufficient size to cover four or five pixels in image space in the horizontal and vertical directions. Black tape may be a convenient and effective means to apply targeting to the wing in the future. Due to the extreme foreshortening of the view caused by the low inclination angle of the camera to the wing of around  $10^\circ$ , it will be desirable to use rectangular targets with an aspect ratio of around four or so with the long axis running in the spanwise direction. Example images for comparison of the FDMS target housings are shown in figure 12 for video and figure 13 for a high-resolution digital still camera planned for future evaluation tests.

Detection of straight edges at known semispan locations was slightly more successful in terms of automation and data quality. Edge detection was found to partially work on the upper edge of the launcher rail located at the wing tip. Edge detection is illustrated in figures 14 and 15 in the form of binary images highlighting the edges automatically found with the *sobel* edge detection method using default settings in the MATLAB® image processing toolbox. Figure 14 is an example of an image with background clutter consisting of clouds and nonuniform illumination on the wing. Figure 15 is an example of a *blue-sky* background image in which the automated edge detector works reasonably well. In order to extract the proper edge, the MATLAB® code was developed that isolated the edge detector output to a region surrounding the launcher rail; the code also tracked the potential edges over an angular range expected to include the desired edge. The results using default edge detector settings are shown in figure 16 where about half of the edge of interest is missed. Selection of the suitable threshold by trial and error leads to the improved results of figure 17, which captures much of the edge. Figure 18 is an example of the edge found on a blue-sky background image. Little tweaking of input parameters is necessary for these relatively high-contrast edges. An example of a noisy edge and automated selection of data representing the edge of interest is shown in figure 19. For that figure the first selection of the edge data is highlighted in red. The data in red are then passed through a filter that rejects data outside of a set fraction or number of standard deviations of the linear least squares computed angle in pixel space and over a range of angles. The

final filtered edge data from which the angle computations are made are indicated in green in figure 19. With this method and operator viewing of the overlaid edges on each image, a data segment of about 11 s was analyzed for launcher rail angle change at the wing tip during which the aircraft passed from level flight through a maneuver and then returned to level flight.

## 4. EXAMPLES OF IN-FLIGHT MEASUREMENTS

### 4.1 Spanwise wing deflection due to aerodynamic loading

Three hundred sixty-one individual digital images at a resolution of  $704 \times 480$  (bitmap .bmp color RGB format) were extracted from a DVD image sequence recorded from a flight-hardened video-monitoring camera that views the left wing of the AAW F/A-18 research aircraft. Thirty-one of the images were from a 1-s time history while the aircraft was on the runway. Three hundred thirty of the images covered the aircraft from level flight ( $M = 0.95$ ,  $q = 750$  psf, altitude = 15,000 ft) through a  $90^\circ$  bank-and-return maneuver over a time period of 11 s. One image each from the runway, level flight, and at the peak of the maneuver was selected for initial measurements. Because some of the FDMS target housings, especially outboard toward the trailing edge of the wing, were barely distinguishable from the background, the image locations of the targets for the three images were manually selected within MATLAB®. The red, green, and blue components of each digital image could be analyzed separately. The red component was found to have highest contrast for most of the images and was used for further analyses. The estimated precision of manual image coordinate location is at best a pixel or so whereas centroiding of high-contrast targets with proper background removal can yield a precision of 0.01 pixel (one standard deviation). The relatively poor precision of the manual image coordinate selection accounts for the large scatter in the results presented below. Larger, higher contrast, better defined targets would allow for automated image processing, such as centroiding, and lead to much less data scatter.

Resection on the level flight image was used to establish the pointing angles and location of the camera in the aircraft coordinate system necessary for the single-camera, single-view solution. The semispan locations ( $X$ -coordinate) of each FDMS target were used to compute  $Y$  (fuselage station) and  $Z$ . The error in these pointing angles and location of the data camera due to resection are not as critical as in some photogrammetric applications. For this application, the image coordinates change very little from condition to condition so that bias errors in the computation of  $Y$ - and  $Z$ -coordinates from equations (6) tend to cancel when the reference condition is subtracted. Figure 20 shows the relative  $Z$ -deflection of the 16 FDMS targets from a level flight condition to a maneuver. The computed  $Z$ -values of the level flight image were subtracted from the maneuver image to arrive at the  $\Delta Z$ -values. For figure 20, the deflection represented by the arrows does not have perspective correction. In other words, the amount of deflection indicated by the arrows is independent of where on the image the arrows are located. The most inboard targets exhibit very little deflection, as expected. The deflection increases as one moves outboard toward the wing tip. The housings nearest the leading edge and closest to the front wing spar had higher contrast, with corresponding better precision than the rest of the housings. The corresponding normalized (to maximum deflection)  $\Delta Z$  is plotted in figure 21 versus normalized semispan  $\eta$ . The solid line in figure 21 is a second-order polynomial fit to the seven targets nearest the leading edge, indicated by circles, which lie along the front wing spar. The midchord row targets (near the rear spar) are indicated with squares and the targets nearest the trailing edge (aft spar) are indicated with diamonds. Although the scatter in these data is relatively large, it does indicate the correct trend and illustrates the potential of useful measurements given low-contrast nonideal targets, even with low-resolution video. It is estimated that an improvement approaching a factor of 10 could be achieved in data precision with larger, better defined, high-contrast targets, even with relatively low-resolution video recording.

### 4.2 Change in twist at wing tip due to aerodynamic loading

Plots of the wing tip angle while on the runway, in level flight, and at maneuver (corresponding to manual image plane measurements on the three images mentioned in section 4.1) are shown in figure 22. Flow is from left to right. The solid lines are first-order linear least-squares fits to each  $Y$ ,  $Z$  data set for each of the three digital images. The dotted lines are  $\pm 1$  standard deviation of the polynomial fits. The characteristic negatively induced wing twist due to aerodynamic loading is evident upon comparing the runway data with level flight data. Very little vertical deflection at the wing tip is noted when comparing runway with level flight data. The main effect of the maneuver is upward deflection of the wing tip and a slight increase in wing twist at the tip. The relatively stable image locations (and corresponding stable spatial object locations) of the most inboard targets mentioned in section 4.1 give credibility that



the nature of the wing tip deformation is effectively depicted in figure 22 rather than camera movement, which would have caused image plane motion of the most inboard targets as well.

In order to assess the precision of angle and deflection measurements, pixel coordinates were determined with image processing of the top edge of the launcher rail and transformed to spatial coordinates for 31 images of the wing (while taxiing on the runway over a 1-s period). See section 3.4 for further details. Due to the relatively stable wing and background while taxiing, this data set serves as an indicator of close to *best-case* angular and deflection measurements over a short time period for this relatively low-contrast video resolution data set. For the runway 1-s data reference set the standard deviation of the measured angles was  $0.020^\circ$ . Note also that the standard deviations of the linear least-squares fits used to determine the slope angle in  $Y, Z$  spaces also had a typical value of  $0.02^\circ$ . The mean angle from this 31-sample set used to subtract out as reference for the following data thus has a standard deviation of about  $0.004^\circ$  ( $0.02/\sqrt{31}$ ). The standard deviation of the  $Z$ -measurements at midchord was 0.032 in. with a corresponding standard deviation of the mean  $Z$ -value used for reference of  $0.006^\circ$ . Background clutter (clouds, etc.), the location of the Sun relative to the wing, and poor contrast in general will cause these best-case values to worsen considerably.

Edge detection image processing was used to record the change in twist and deflection at the wing tip (top edge of the launcher rail) as a function of time. The normalized change in wing tip twist as a function of time from level flight through maneuver and back to level flight is shown in figure 23 for an 11-s record. The data for this plot (and figure 24 as well) were obtained in a piecewise fashion because no single edge detector with default input parameter worked well for the entire time sequence. Although complete automated image processing was not achieved for the entire time sequence, the piecewise reduction time history is encouraging for future development efforts. Figure 24 shows the corresponding change in  $Z$  at the midpoint of the tip chord for the same time sequence as figure 23. The heavy lines in both figures 23 and 24 show a five-sample moving average used to smooth the data. The lines plotted near zero in each figure show the relative precision (two times the standard deviation) of each linear fit used to create the plots versus time. The relative precision is noticeably worse for images with background clutter and poor contrast.

It can be noted from figure 23 that, at the end of the maneuver, the wing tip twist did not return to its premaneuver value. This start-to-finish difference is several times as large as the relevant data uncertainty levels and therefore indicates that the wing took a “set” during the maneuver. It is known that the F/A-18 wing does this. When the AAW wing was load tested to quantify its torsional stiffness, as reported in reference 11, the wing’s structural hysteresis was noted. This hysteresis is due to the aggregate effect of many mechanically fastened joints, each with fitting tolerance and friction. That this effect is not apparent in figure 24 is attributed to the fact that the vertical displacement was measured for a point near the wing’s elastic axis.

## 5. CONCLUSIONS

The single-camera, single-view photogrammetric method is shown to be useful for the measurement of static and dynamic aeroelastic wing deformation of aircraft in flight. The primary advantages of the single-camera, single-view technique are: (1) only one camera is needed, reducing space and viewport requirements on the aircraft, (2) the base separation of multiple cameras (with necessary suitable locations) is not a factor, and (3) the coordinate taken as known (to allow a single-camera solution) can usually be obtained with more accuracy pretest than is possible with multicamera photogrammetry during in-flight data taking. Actual in-flight measurements of the AAW F/A-18 research aircraft illustrate that useful measurements are possible from a standard resolution video camera with low-resolution targets. An improvement in precision by a factor of 10 is anticipated for high-contrast targets. Time-history examples of changes in induced twist angle and deflection show the improvement in measurement precision possible with image processing of lines or edges located at various semispan stations. Although complete automated image processing was not achieved for the entire time sequence, the results of the piecewise reduction time history are encouraging for future developmental efforts.

## ACKNOWLEDGMENTS

The support and technical assistance of team members of the Active Aeroelastic Wing program, the Aerostructures Branch at Dryden Flight Research Center, and the Instrumentation Systems Development Branch at Langley Research Center are acknowledged.

## REFERENCES

1. V. Michael DeAngelis and Robert Fodale, "Electro-Optical Flight Deflection Measurement System," *Society of Flight Test Engineers 18th Annual Symposium Proceedings*, SFTE Technical Paper 22, pp. 1-14, Sept. 1987.
2. Kenneth L. Bonnema and William A. Lokos, "AFTI/F-111 Mission Adaptive Wing Flight Test Instrumentation Overview," *ISA 35th International Instrumentation Symposium*, Paper #89-0084, pp. 809-839, May 1989.
3. William A. Lokos, "Predicted and Measured In-Flight Wing Deflections of a Forward-Swept-Wing Aircraft," *NASA TM-4245*, 21 pp., Jan. 1990.
4. William A. Lokos, Catherine M. Bahm, and Robert A. Heinle, "Determination of Stores Pointing Error Due to Wing Flexibility Under Flight Load," *AIAA 7th Biennial Flight Test Conference*, AIAA 94-2112, 20 pp., June 1994.
5. P. Williard, J. D. Hardin, and J. H. Whitehead, "Determination of In-Flight Aeroelastic Deformation of a Transport High-Lift System Using Optical Position Measurement Technology," *1<sup>st</sup> AIAA Aircraft Engineering Technology and Operations Congress*, Los Angeles, CA, Sept. 19-21, 1995.
6. A. W. Burner and Tianshu Liu, "Videogrammetric Model Deformation Measurement Technique," *J. of Aircr.*, **38**, 4, pp. 745-754, July-August 2001.
7. E. M. Mikhail, J. S. Bethel, and J. C. McGlone, *Introduction to Modern Photogrammetry*, chapt. 9, John Wiley & Sons, New York, 2001.
8. E. Pendleton, K. E. Griffin, M. Kehoe, and B. Perry, "A Flight Research Program for Active Aeroelastic Wing Technology," AIAA Paper No. 96-1574, *37th AIAA Structures, Structural Dynamics, and Materials Conference*, Salt Lake City, Utah, pp. 2263-2273, April 1996.
9. E. Pendleton, D. Bessette, P. Field, G. Miller, and K. Griffin, "The Active Aeroelastic Wing Flight Research Program, Technical Program & Model Analytical Development," *J. of Aircr.*, **37**, 4, pp. 554-561, July-August 2000.
10. A. W. Burner, Tianshu Liu, and Richard DeLoach, "Uncertainty of Videogrammetric Techniques Used for Aerodynamic Testing," *22nd AIAA Aerodynamic Measurement Technology and Ground Testing Conference*, St. Louis, Missouri, AIAA 2002-2794, 20 pp., June 2002.
11. William A. Lokos, Candida D. Olney, Natalie D. Crawford, Rick Stauff, and Eric Y. Reichenbach, "Wing Torsional Stiffness Tests of the Active Aeroelastic Wing F/A-18 Airplane," AIAA-2002-1333, 9 pp., Jan. 2002.



Figure 1: F/A-18 Active Aeroelastic Wing research aircraft.



Figure 2: Camera pod and left wing.



Figure 3: Camera pod viewports.

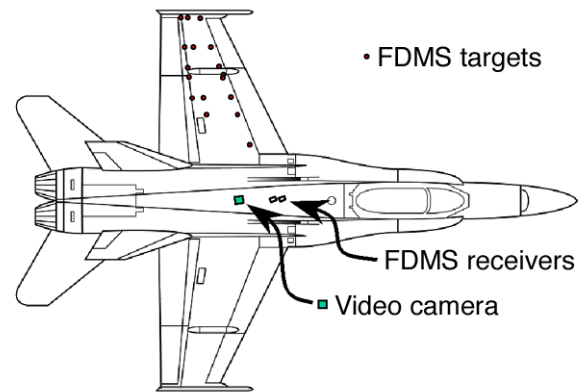


Figure 4: Planview with video camera, FDMS receivers, and targets indicated (circles).

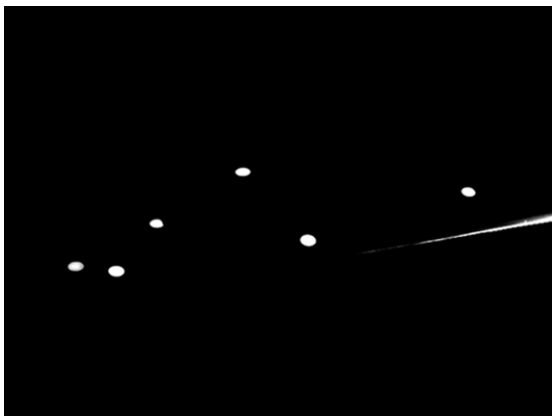


Figure 5: Example of high-contrast image during wind tunnel testing.



Figure 6: Image locations during level flight (circles) compared with alternate, incorrect resection solution (+'s).



Figure 7: Image locations during level flight (circles) compared with correct resection solution (+'s).



Figure 8: Resection residuals in image space.



Figure 9: Error in  $\Delta Z$  based on resection residuals.



Figure 10: Error in  $\Delta Z$  due to a 1-pixel error in vertical image coordinate.



Figure 11: Error in  $\Delta Z$  due to a 1-pixel error in horizontal image coordinate.



Figure 12: Video image of FDMS target housing.





Figure 13: High-resolution digital still camera image of FDMS target housing.



Figure 14: Binary image showing edges found after processing "poor" image.



Figure 15: Binary image showing edges found after processing "good" image.

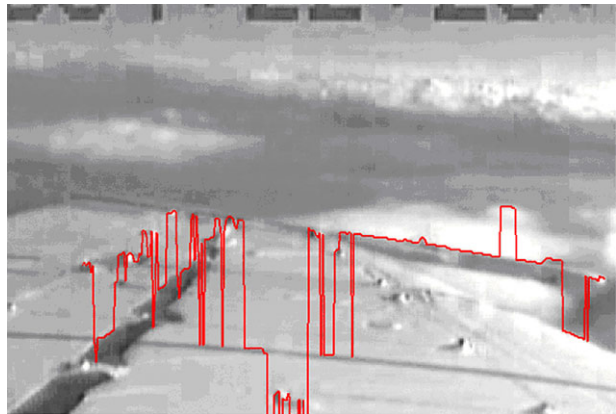


Figure 16: Enlargement of "poor" edge processing.



Figure 17: Better edge processing of "poor" image.

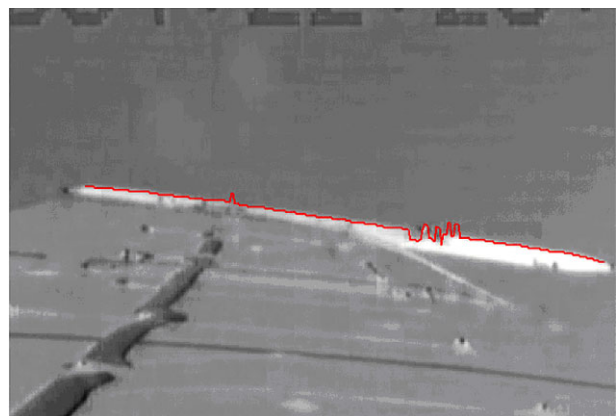


Figure 18: Edge processing of "good" image.

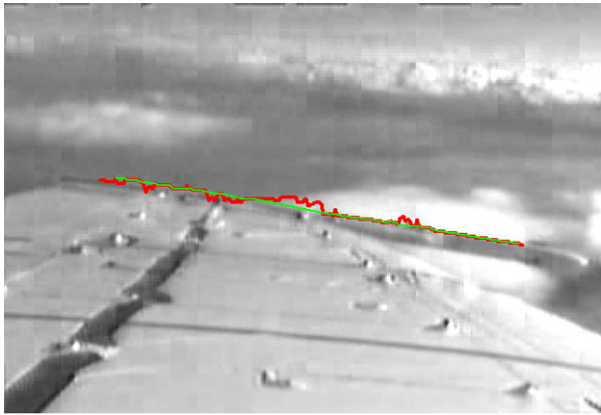


Figure 19: Example of selection and rejection of edge data for image with background clutter.



Figure 20: Relative Z-deflection from level flight to maneuver.

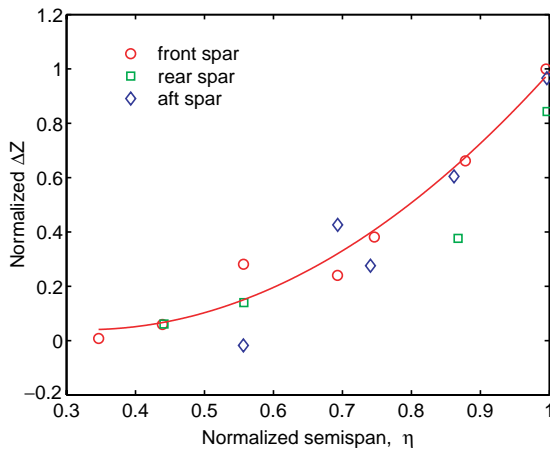


Figure 21: Normalized deflection versus semispan.

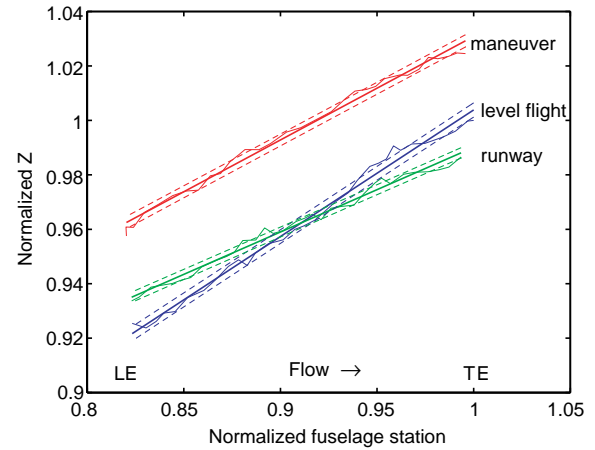


Figure 22: Launcher rail relative position for runway, level flight, and maneuver.

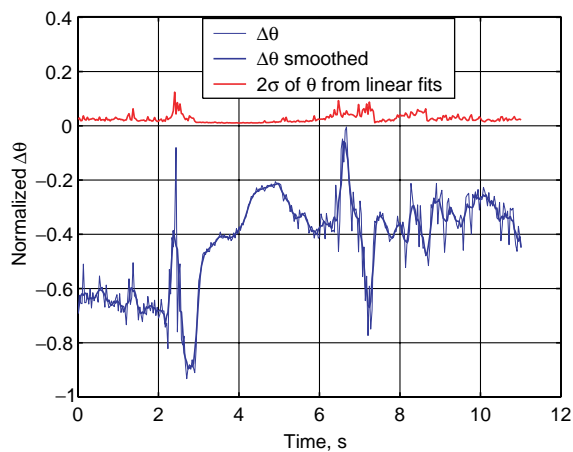


Figure 23: Normalized change in launcher rail angle versus time during maneuver.

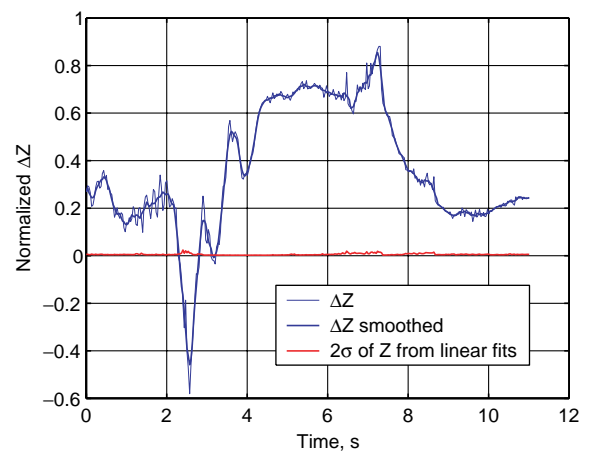


Figure 24: Normalized change in Z of launcher rail versus time during maneuver.